Electronic Supplementary Material (ESI) for Journal of Materials Chemistry C.

Supplementary information for

Ultrasensitive broadband photodetectors based on two-dimensional Bi_2O_2Te films

Authors: Pin Tian,[a,b] Hongbo Wu, [c] Libin Tang,[*a,b] Jinzhong Xiang,[b,d] Rongbin Ji,[a] Shu Ping Lau, [*e] Kar Seng Teng, [*f] Wei Guo, [*c] Yugui Yao[*c] and Lain-Jong Li[g]

Address:

[a]Kunming Institute of Physics, Kunming 650223, P.R. China.

[b]Yunnan Key Laboratory of Advanced Photoelectric Materials & Devices, Kunming 650223, P.R. China.

[c]Beijing Key Laboratory of Nanophotonics and Ultrafine Optoelectronic Systems and Micro-nano Centre, School of Physics, Beijing Institute of Technology, Beijing 100081, China.

[d]School of Physics and Astronomy, Yunnan University, Kunming 650091, P.R. China.

[e]Department of Applied Physics, The Hong Kong Polytechnic University, Hong Kong SAP, P.R. China.

[f]College of Engineering, Swansea University, Bay Campus, Fabian Way, Swansea SA1 8EN, United Kingdom.

[g]School of Materials Science and Engineering, University of New South Wales, Sydney 2052, Australia. *email: sscitang@163.com

Table of Contents

S6. Discussion on lattice distance and crystal orientation of Bi_2O_2Te.

S7. Discussion on transient response time of photodetector based on 2D Bi_2O_2Te.

S8. Discussion on relevant parameters of photodetector based on 2D Bi_2O_2Te.

S9. Table on a list of Hall measurements on sputtered Bi_2Te_3 (Table S2).

S1. Band structures of 2D Bi_2O_2Te film as a function of thickness by theoretical calculation.

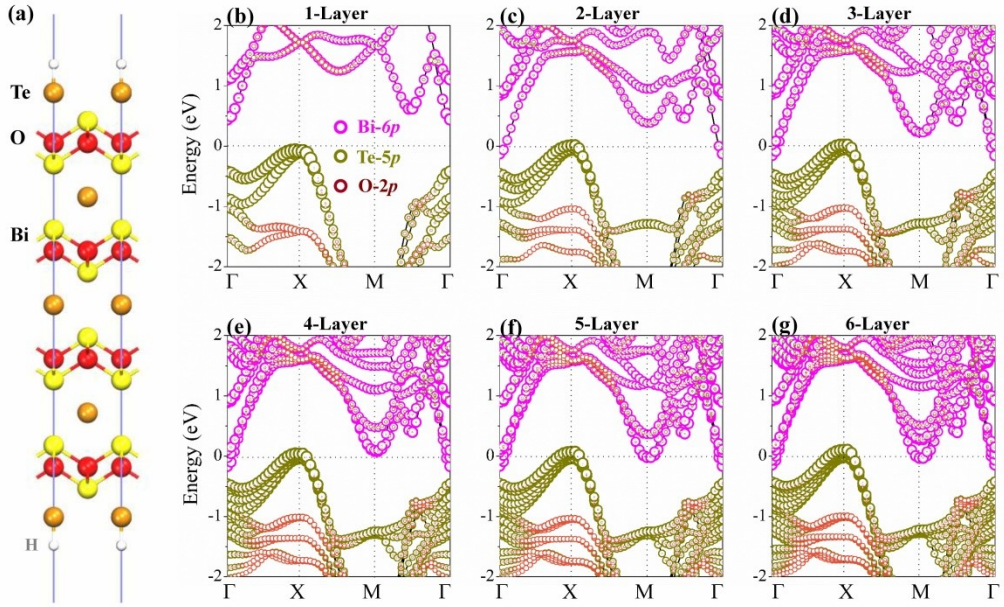

Fig. S1. Electronic structures of 2D layered Bi_2O_2Te. (a) The atomic structures of 2D layered Bi_2O_2Te film with four-layer thickness. (b-g) Evolution of the band structures of 2D layered Bi_2O_2Te ranging from monolayer to six layers. The pink, dark-yellow, and orange circles represent contributions of Bi-6*p*, Te-5*p*, and O-2*p* orbitals, respectively. The Fermi level is shifted to zero.

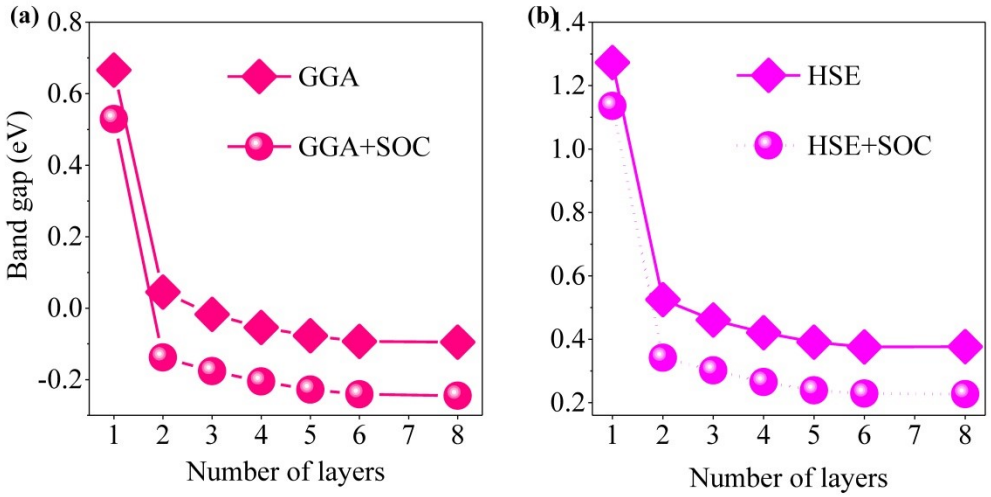

Fig. S2. Evolution of the indirect bandgaps of Bi_2O_2Te as a function of film thickness. Left panel: PBE vs PBE+SOC. Right panel: HSE vs HSE+SOC.

S2. Study of transition from Bi_2Te_3 to Bi_2O_2Te.

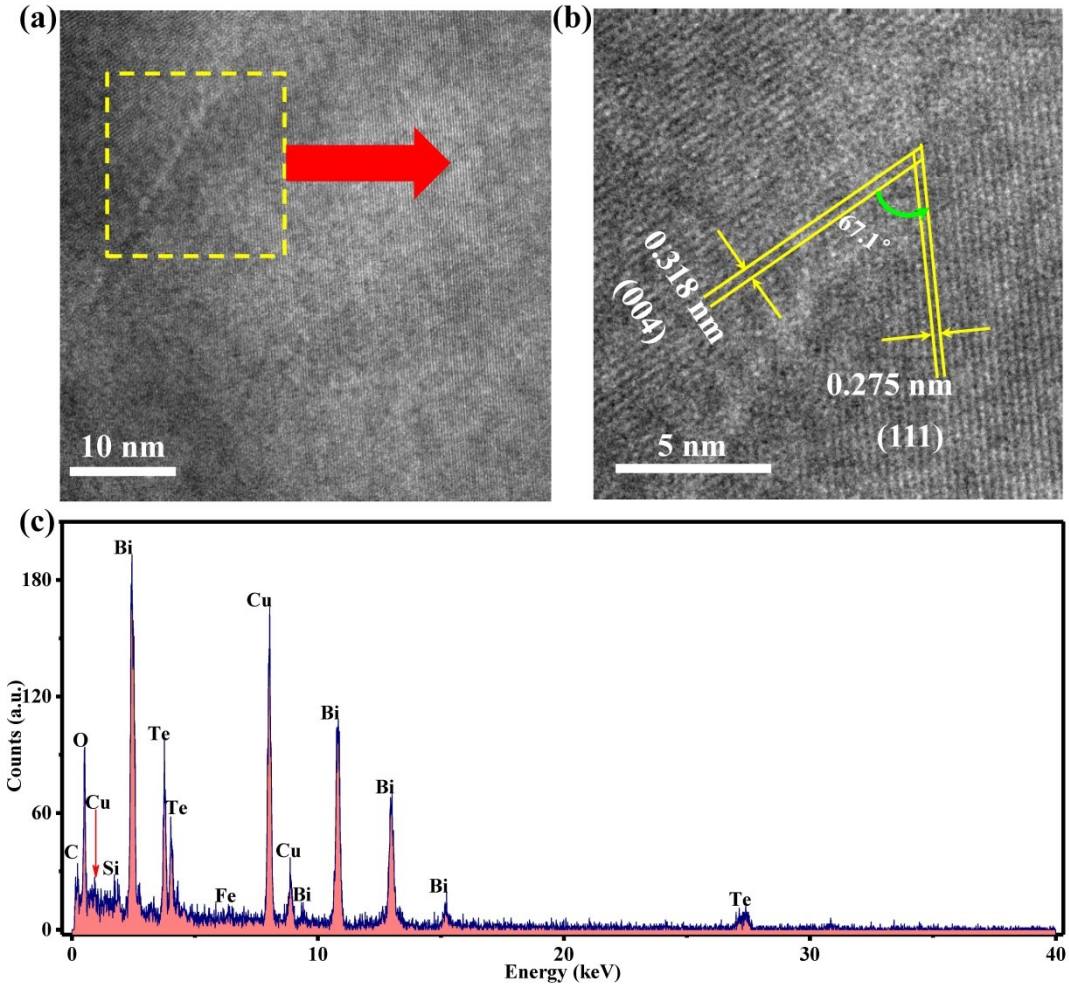

Fig. S3. Structural characterization of Bi_2O_2Te thin film. (a) Transmission electron microscope (TEM) image of as-prepared Bi_2O_2Te film. (b) High-resolution TEM (HRTEM) image of highlighted area in (a) showing crystal spacing of 0.318 and 0.275 nm along (004) and (111), respectively and grain boundary angle of 67.1°. (c) Energy dispersive spectroscopy (EDS) analysis of Bi_2O_2Te thin film.

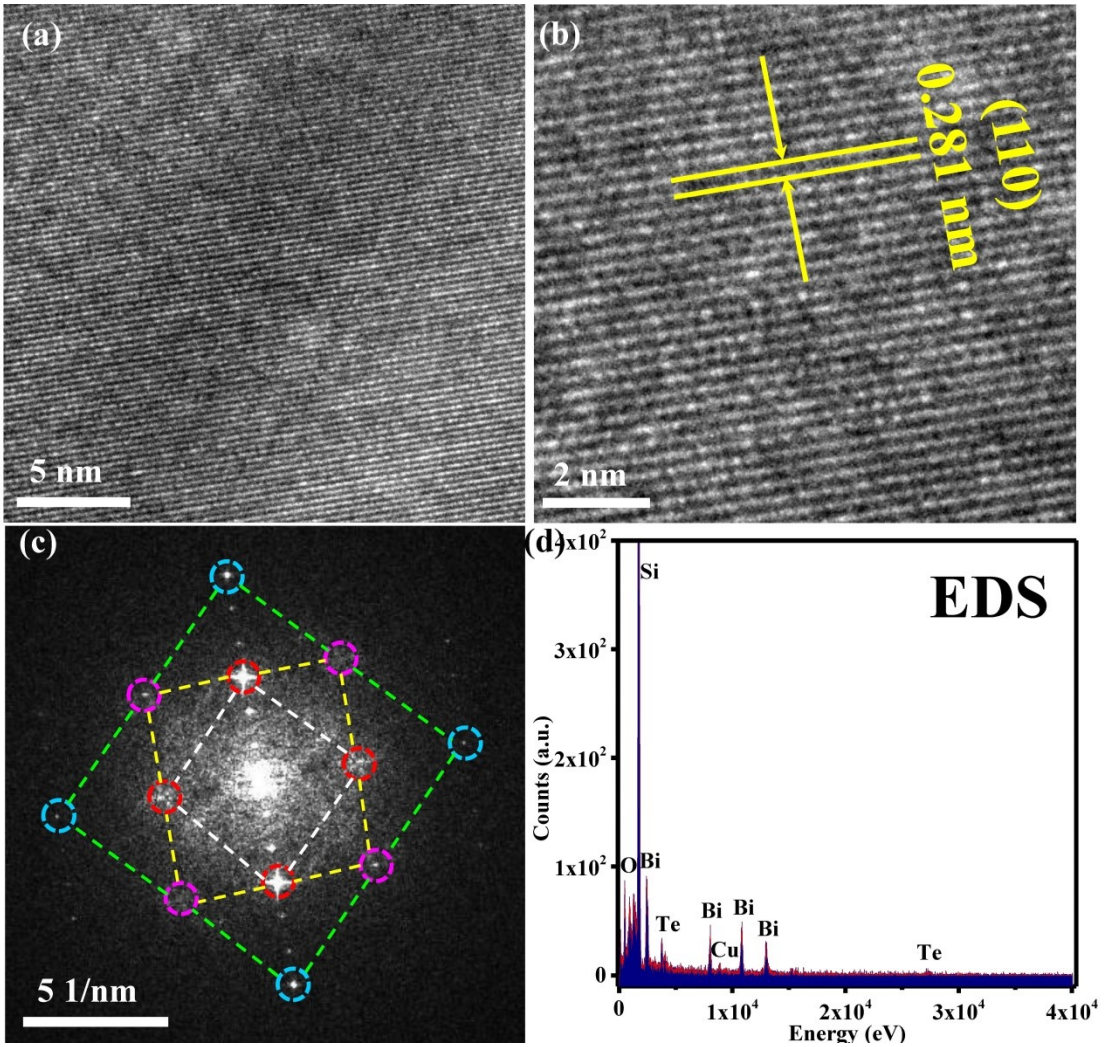

Fig. S4. HRTEM characterization of Bi_2O_2Te thin film. (a) HRTEM images of Bi_2O_2Te thin film prepared by transition of Bi_2Te_3. (b) HRTEM image showing lattice fringes with separation of 0.281 nm along (110), enlarged from (a). (c) The fast fourier transform (FFT) image of (a), and the patterns indicate that the crystal is of square structure. (d) Energy dispersive spectroscopy (EDS) of Bi_2O_2Te thin film showing the presence of Bi, O and Te elements. Si and Cu peaks were also appeared in the spectrum due to Si substrate and Cu grids, respectively.

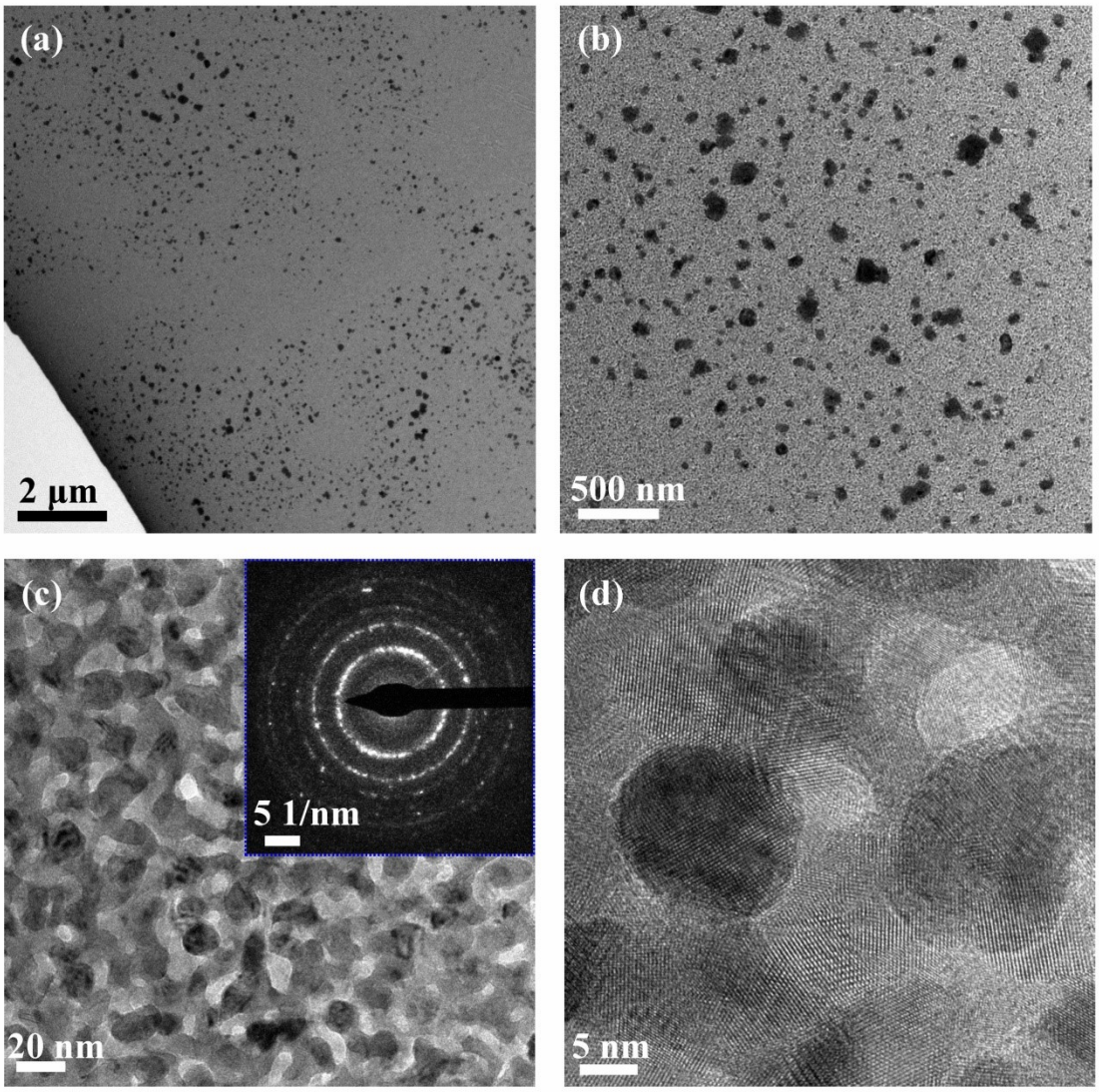

Fig. S5. TEM characterization of Bi_2Te_3 thin film prepared by sputtering. (a-b) Morphology of Bi_2Te_3 thin film prepared by sputtering. (a) Low magnification of the film prepared by sputtering. (b) Image showing some dark spots on the thin film due to the direction of deposition, which the substrate was directly below to target. (c) HRTEM image of Bi_2Te_3 thin film comprising of dense single crystal snowflake-like structures. The inset of (c) indicates that the thin film is of polycrystalline structure. (d) HRTEM image showing lattice fringes at the polycrystalline structure.

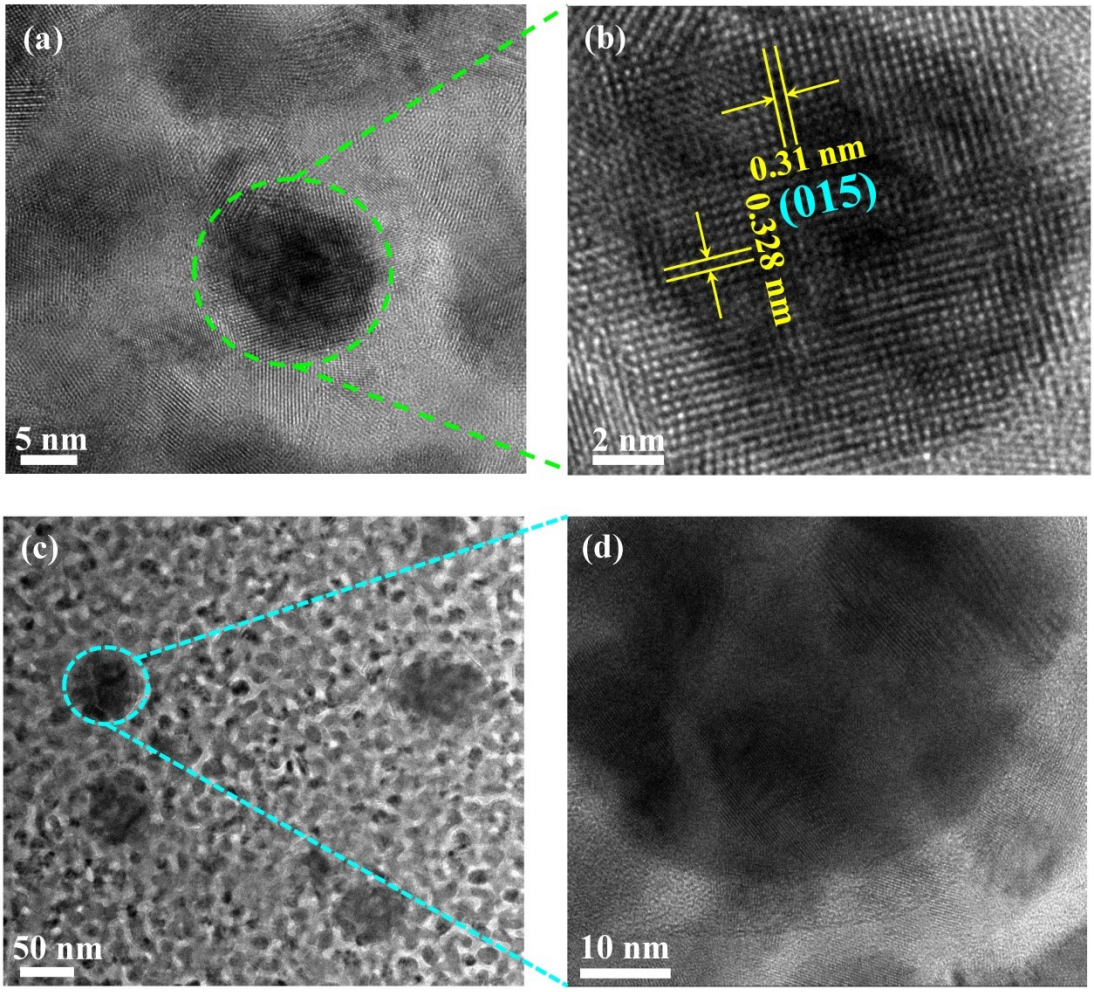

Fig. S6. HRTEM characterization of Bi_2Te_3 thin film prepared by sputtering. (a-b) HRTEM images of Bi_2Te_3 thin film prepared by sputtering. (a) HRTEM image of uniform film, and (b) image showing lattice fringes with separation of 0.31 and 0.328 nm along (015), which was enlarged from the green circle in (a). (c) HRTEM images showing dark spots on the uniform film, and (d) HRTEM image showing lattice fringes, enlarged from cyan circle in (c).

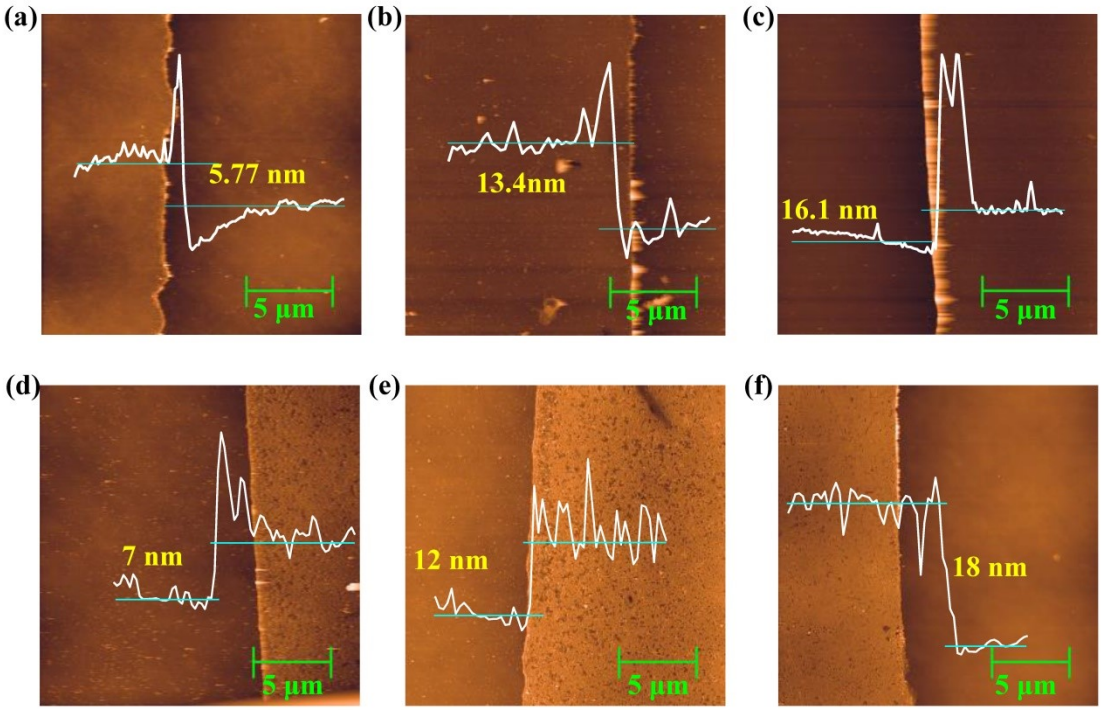

Fig. S7. AFM measurements on the thickness of Bi_2Te_3 and Bi_2O_2Te films prepared under various conditions. (a-c) The thickness of Bi_2Te_3 prepared with sputtering duration of 5 s (a), 10 s (b) and 15 s (c) while keeping other parameters constant. (d-f) The thickness of Bi_2O_2Te prepared with Bi_2Te_3 sputtering duration of 5 s (d), 10 s (e) and 15 s (f) followed by rapid annealing at 400℃ for 10 min.

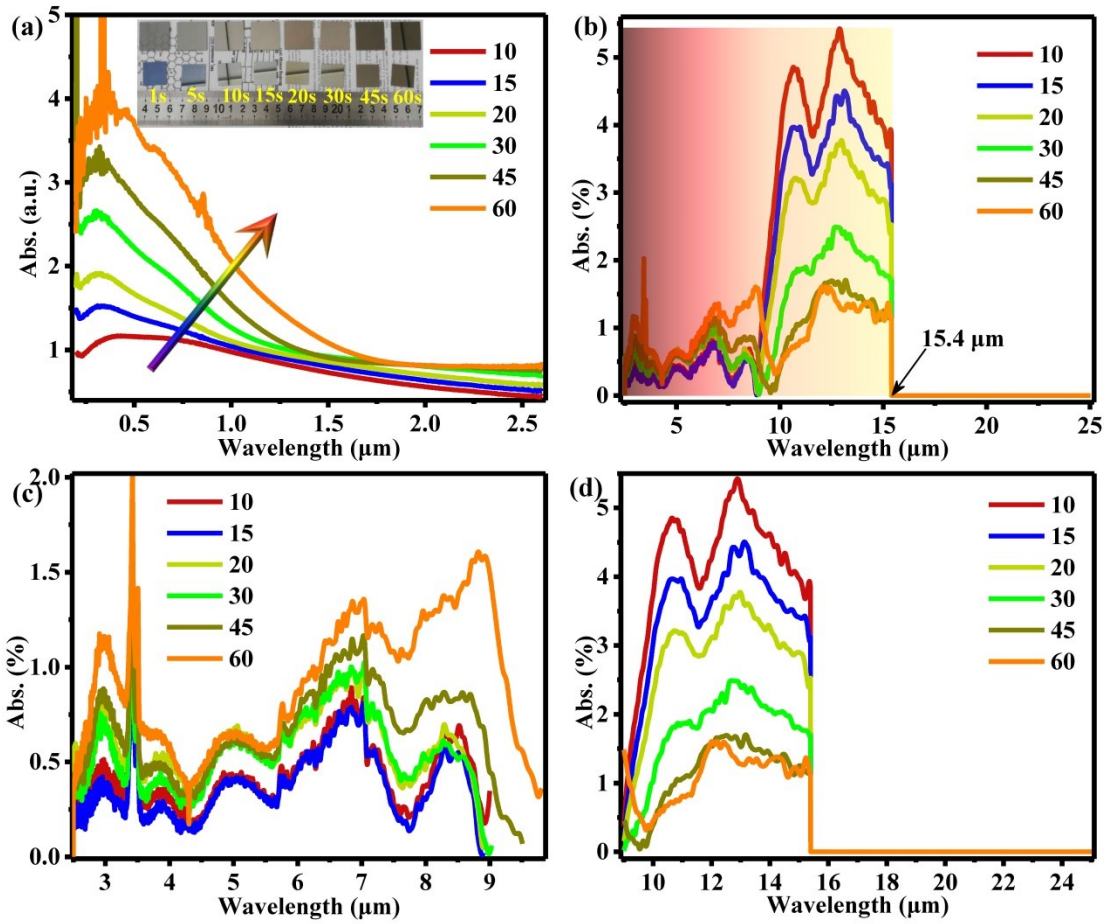

Fig. S8. Optical characterization of sputtered Bi_2Te_3 thin film. (a) UV-visible near infrared absorption spectrum of Bi_2Te_3 thin film with different sputtering duration of 10, 15, 20, 30, 45 and 60 s. Inset shows optical images of Bi_2Te_3 grown on quartz (top panel) and Si/SiO_2 (bottom panel) substrates by sputtering for 1, 5, 10, 15, 20, 30, 45 and 60 s from left to right. The size of substrates was about 2 cm x 2 cm. (b) The Fourier transform-infrared attenuated total reflection (FTIR-ATR) spectra of the Bi_2Te_3 with different sputtering durations of 10, 15, 20, 30, 45 and 60 s. (c,d) Change in absorption density for various thickness film was similar to the UV-visible near infrared absorption below 9.8 μm (c), the variation trend was contrasted beyond 9.8 μm (d), which attributed to the absorption of quartz substrate.

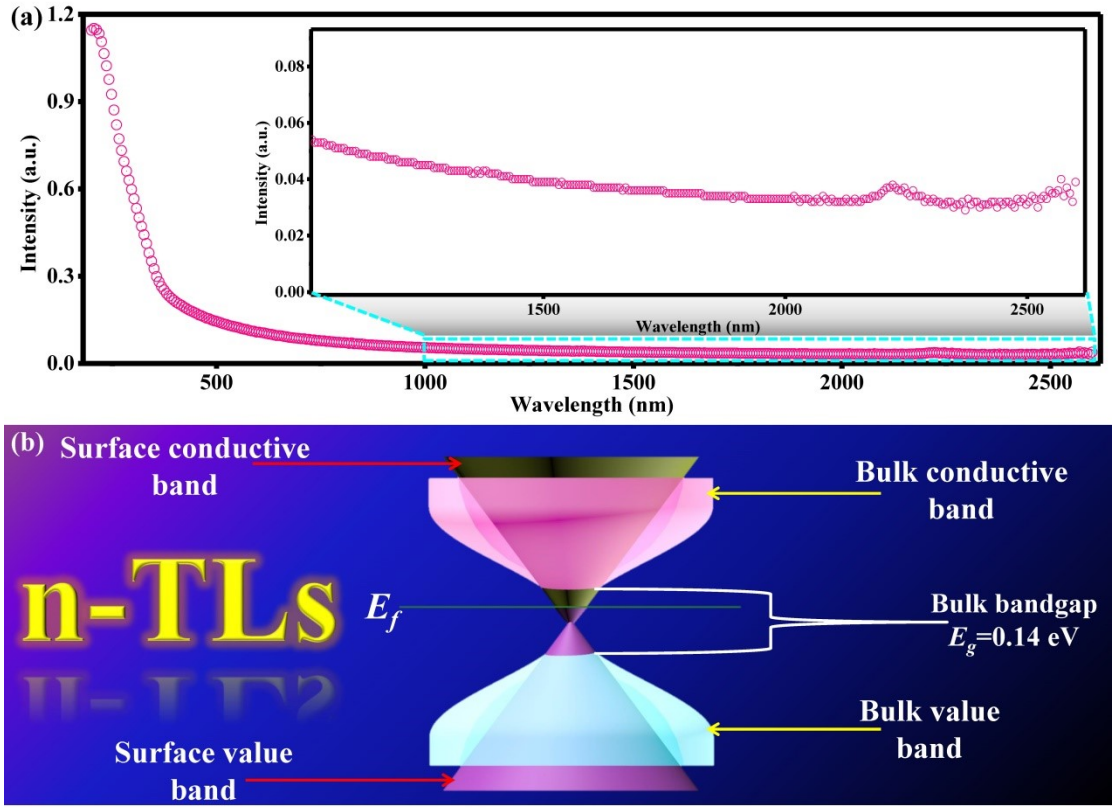

Fig. S9. Optical characterization of Bi_2O_2Te thin film and optical bandgap of Bi_2Te_3 film. (a) UV-visible near infrared absorption spectrum of Bi_2O_2Te thin film by transition of Bi_2Te_3 with sputtering duration of 1 s. Inset shows the enlarged absorption spectrum ranged from 1000 to 2600 nm. (b) The schematic optical bandgap of Bi_2Te_3 thin film based on the calculation of FTIR-ATR absorption spectrum (see Discussion for detailed calculation). Bi_2Te_3 has bulk states (bandgap $\approx$ 0.14 eV) and gapless surface states due to topological characterization.[1] Furthermore, the Fermi energy is above the conduction band due to the n-type nature of Bi_2Te_3 semiconductor according to the Hall measurement results (see Table S2).

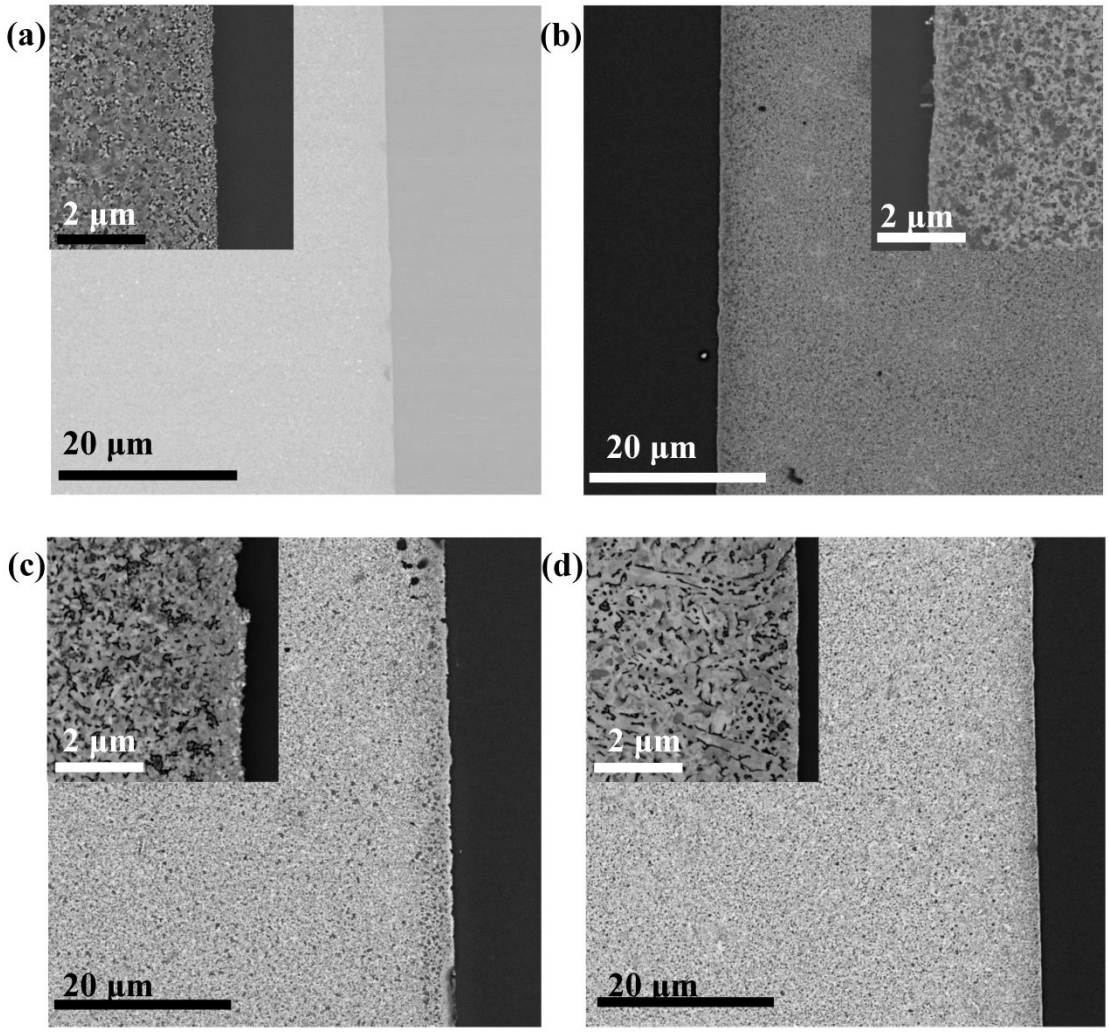

Fig. S10. SEM images of 2D Bi_2O_2Te at various sputtering conditions. (a-d) SEM images of 2D Bi_2O_2Te by transition of Bi_2Te_3 prepared by sputtering for 1 (a), 5 (b), 10(c) and 15 s(d) followed by annealing at 400 ℃ under air atmosphere. All insets show enlarged images revealing uniform and dense films. Besides, the surface texture become denser and the microstructures grew larger in size with increasing sputtering time.

S3. Characterization of photodetector based on 2D Bi_2O_2Te and Si substrate.

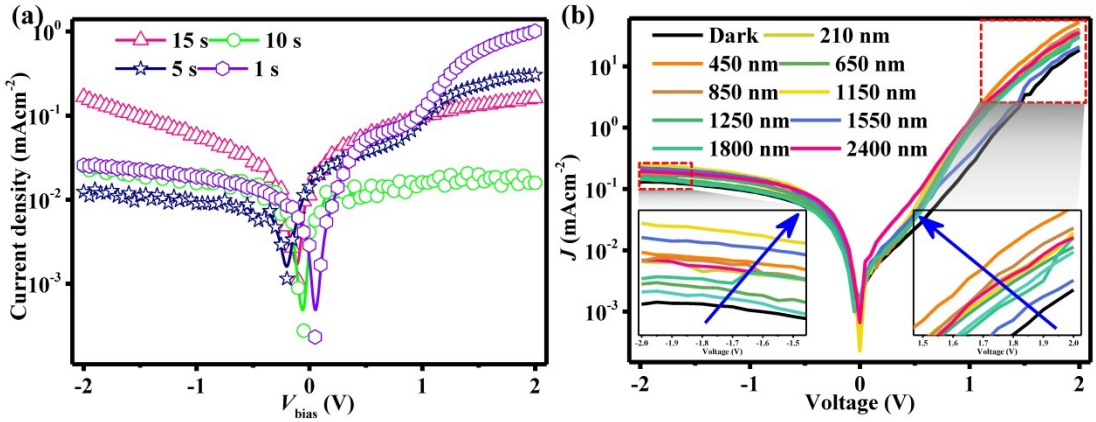

Fig. S11. Rectification characteristics and *J-V* measurements of photodetector based on 2D Bi_2O_2Te. (a) Rectification characteristics of photodetector based on 2D Bi_2O_2Te by transition of Bi_2Te_3 prepared by sputtering for 1, 5, 10 and 15s followed by annealing at 400 ℃ under air atmosphere. The results indicate small rectification for increasing sputtering duration. (b) The *J-V* results of photodetector based on the thinnest 2D Bi_2O_2Te under weak light illumination. Two insets show the increase of current density under weak light illumination ranged from 210 to 2400 nm, which indicate that this device demonstrated good response to weak lights.

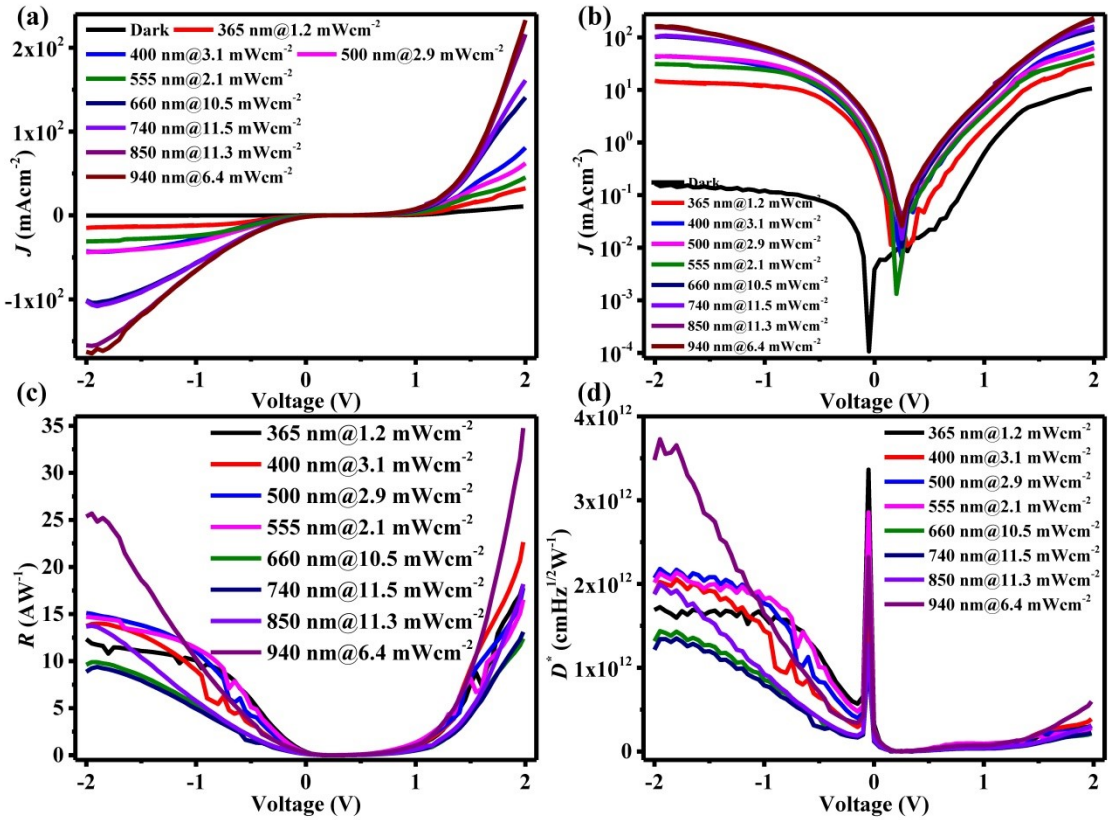

Fig. S12. Performance characterization of photodetector based on 2D Bi_2O_2Te. (a-b) *J-V* curves of photodetector based on the thinnest 2D Bi_2O_2Te under strong light illumination using LEDs. An increase in current density was evident as compared to dark current density (b). (c) and (d) show the *R* and D^* vs voltage curves, respectively.

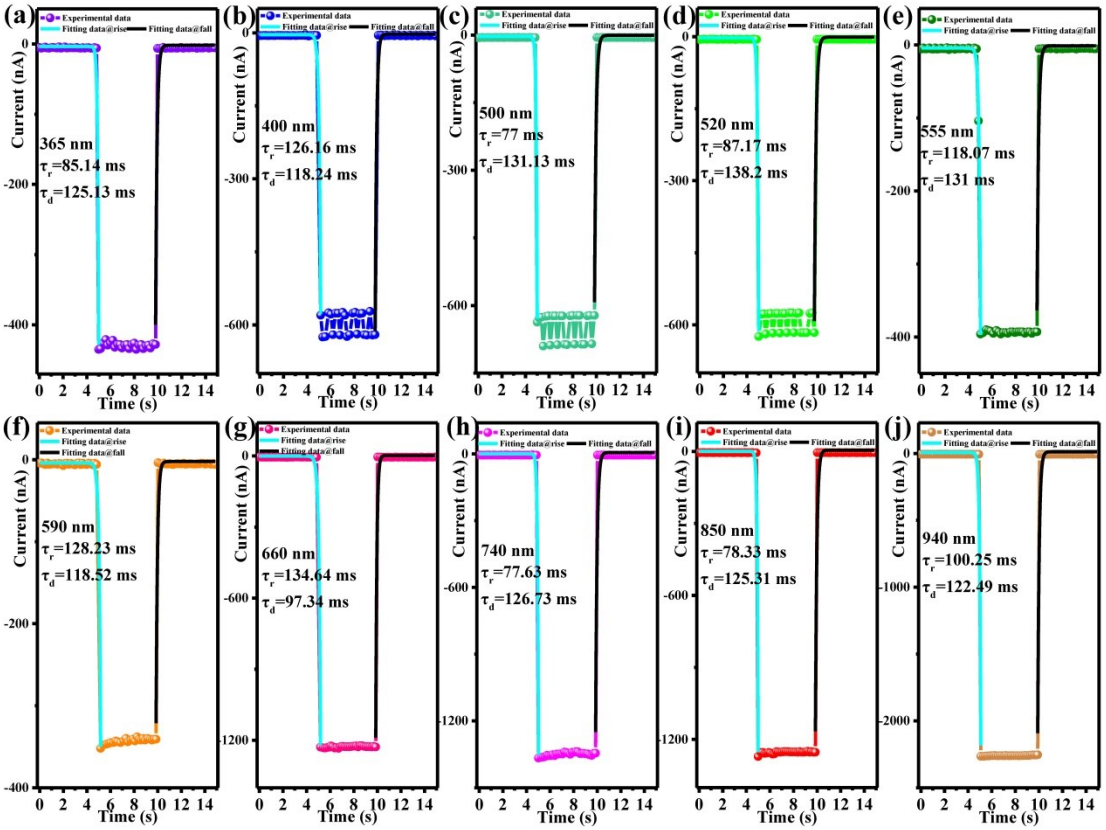

Fig. S13. The transient response characteristics of photodetector based on 2D Bi_2O_2Te. (a-j) The transient response curves of photodetector based on the thinnest 2D Bi_2O_2Te under strong light illumination using LEDs with wavelength of 365 (a), 400 (b), 500 (c), 520 (d), 555 (e), 590 (f), 660 (g), 740 (h), 850 (i) and 940 nm (j). The response time for each wavelength was calculated. Please see Discussion S7 for the detailed calculation.

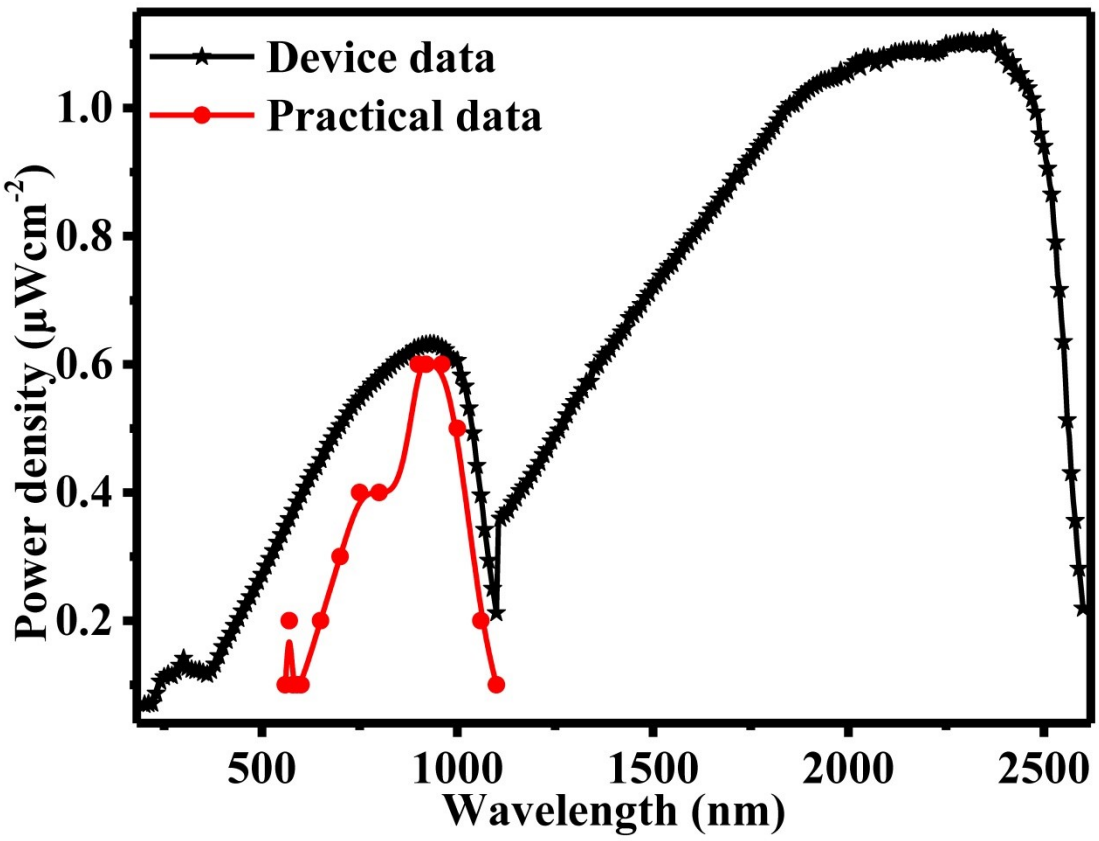

Fig. S14. The power density vs wavelength of weak light sources. Red line represents the power density curves measured using bolometer and black line represents the power density curves obtained from the light source system.

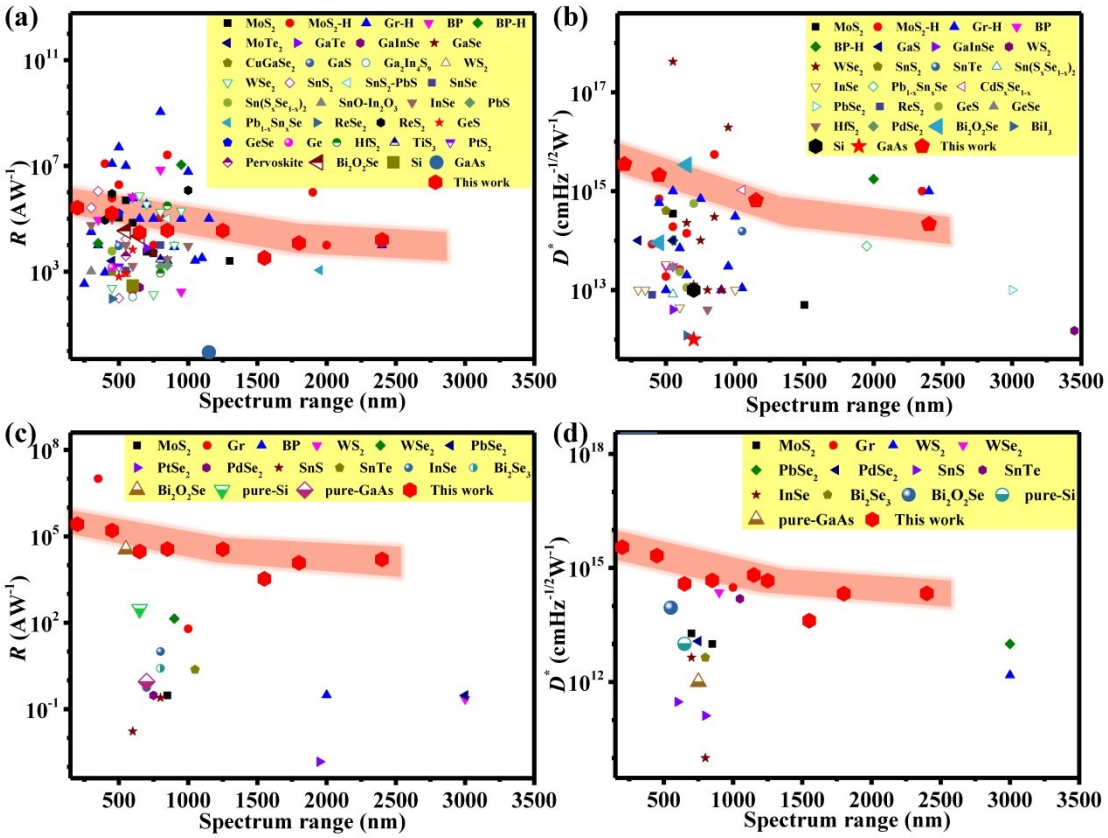

Fig. S15. Comparison on performances of photodetectors based on different 2D materials. Comparison on responsivity (a) and detectivity (b) of photodetectors based on different 2D materials and 2D Bi_2O_2Te (in this work) as well as traditional Si and GaAs photodetectors. Comparison on responsivity (c) and detectivity (d) of photodetectors based on Si hybrid with different 2D materials and 2D Bi_2O_2Te (in this work) as well as traditional Si and GaAs photodetectors. Data are extracted from ref. 2-43.

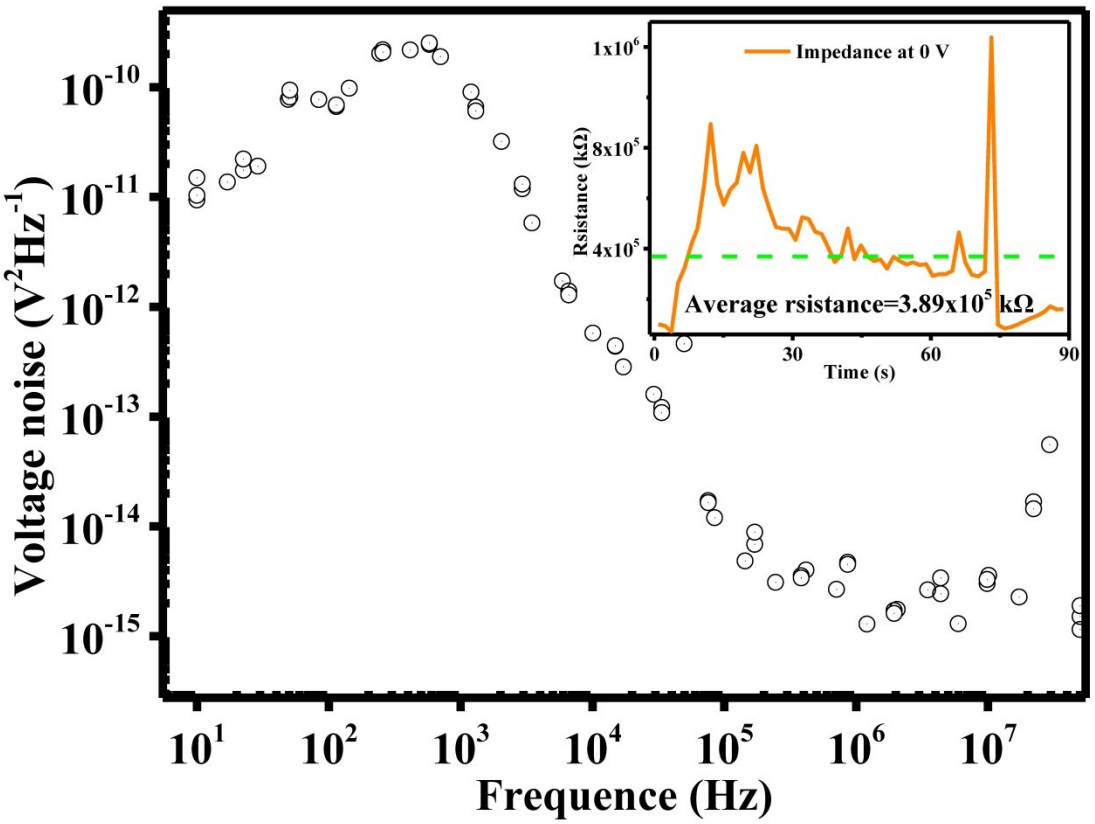

Fig. S16. Spectra of voltage noise power density at 0 V. Inset shows the resistance curve of device at 0 V, which the average resistance of the photodetector is about 3.89x10^8 Ω.

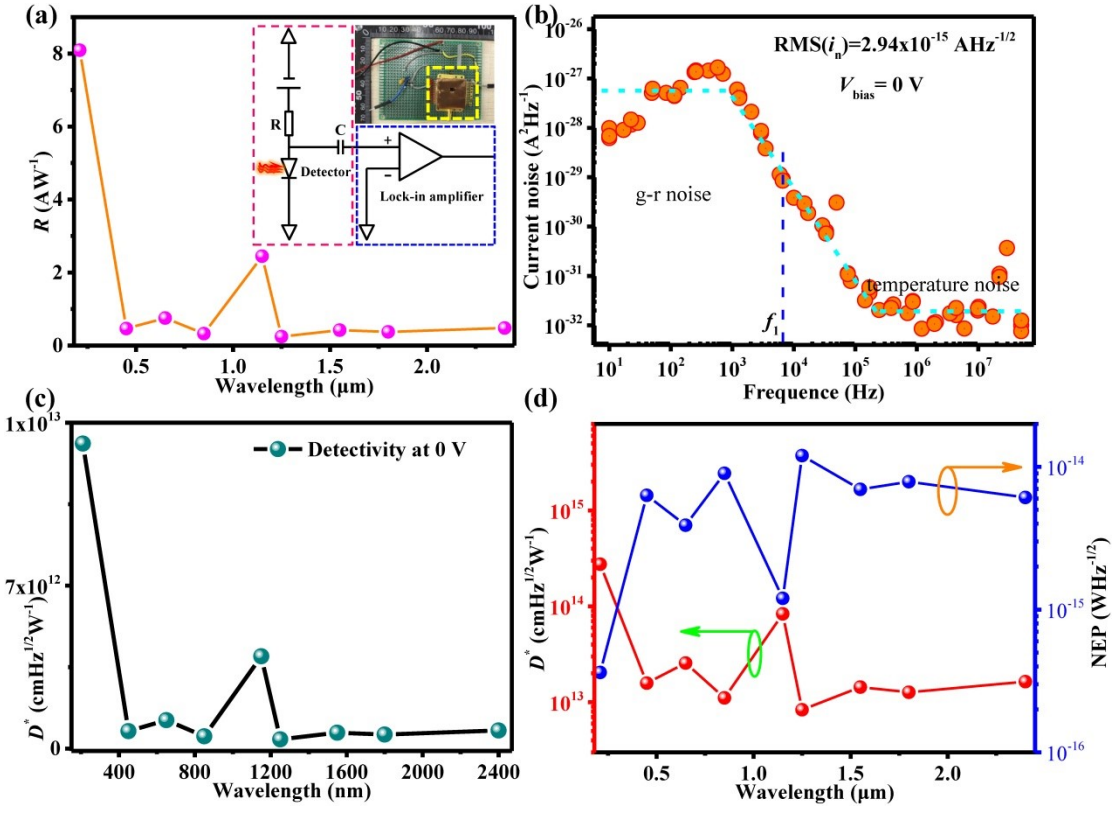

Fig. S17. Relevant parameters of photodetector based on 2D Bi_2O_2Te. (a) Responsivity spectrum of photodetector based on 2D Bi_2O_2Te at 0 V according to the calculation of *J-V* curves under direct current (DC) mode. Inset shows the circuit diagram and optical image of the device, which operated in alternating current (AC) mode. (b) Spectra of current noise power density at 0 V. (c) A plot of detectivity against light wavelengths for the 2D Bi_2O_2Te based photodetector at 0 V according to the calculation of *J-V* curves under direct current (DC) mode. (d) Graphs showing the detectivity (red dash-dotted line) and noise equivalent power density (blue dash-dotted line) against light wavelengths for the 2D Bi_2O_2Te based photodetector at 0 V according to the calculation of noise spectrum and responsivity under AC mode. Please see Discussion S8 for the detailed calculations.

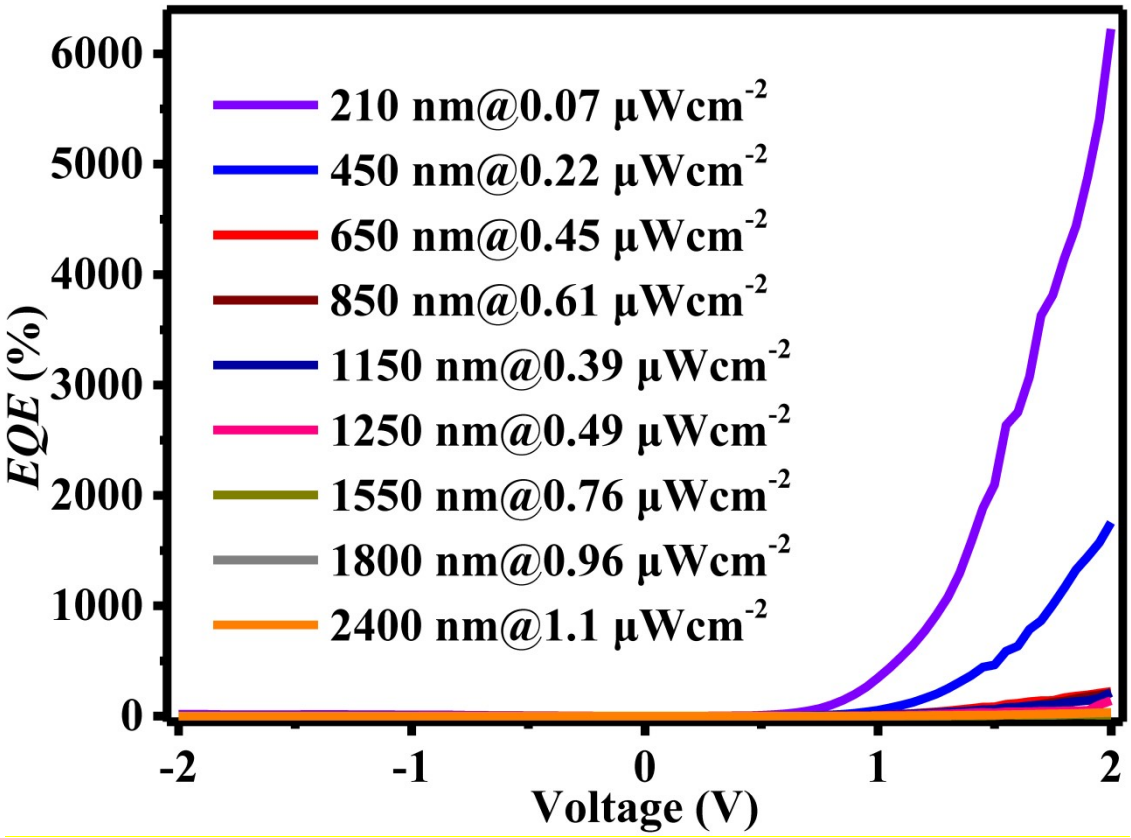

Fig. S18. External quantum efficiency (*EQE*) of photodetector based on 2D Bi_2O_2Te under illumination with various wavelengths.

S4. Discussion on the variation of bandgap with film thickness.

Fig. S1 summarizes the evolution of the band structures of 2D Bi_2O_2Te film as a function of thickness. Here, for computation efficiency, the calculations were performed at GGA+SOC level, focusing on the orbital contribution and evolution

tendency to provide qualitative physics insight. The CBMs and VBMs of Bi_2O_2Te thin film are located at Γ and X, respectively. Close to the Fermi level, the CBM states at Γ and VMB states at X mainly originate from Bi *6p*-orbital states and the Te *5p*-orbital states, respectively. Similar to the layer-dependent band structure evolution feature of few-layer black phosphorus, [44] an increasing 2D Bi_2O_2Te films thickness will lead to stronger interlayer interaction, hence resulting in stronger dispersions of CBMs and VBMs and tunable bandgap with varying film thickness. However, due to the underestimation of the bandgap from PBE (about ~0.5 eV in this case), the closing bandgap is re-opened after using the hybrid functional, which is discussed in the next paragraph.

In Fig. S2, both PBE-GGA and HSE bandgap results are shown for comparison. The standard hybrid functional (e.g. 25% Hartree-Fock and 75% PBE-GGA) calculations employ a screened Coulomb potential for the exchange interaction, which will enhance the bandgap. Although the HSE method opens the bandgap of ~0.5 eV, it is almost a constant correction and the trends of dependence of bandgap on thickness are in good agreement with PBE-GGA values.[45] Because of the strong SOC effect of Bi and Te atoms, the bandgap is decreased by ~0.15 eV. Due to the well-known quantum confinement effect, the bandgaps of 2D Bi_2O_2Te thin film show classic thickness-dependence for all the calculations shown in Fig. S2. The hydrogen passivation effect at the outer most layers of the 2D Bi_2O_2Te structures has caused a dramatic decrease in the bandgap from monolayer to 2 layers. Then, the bandgap gradually decreases and reaches convergence at about ~6 layers (e.g. thickness ~

40Å), in consistent with the experimental observation.

S5. Discussion on calculation of indirect and direct bandgap semiconductor.

The optical absorption is mainly attributed to lattice absorption of crystal. However, the semiconductors can be divided into indirect and direct bandgap semiconductor dependent on the alignment of its VBM and CBM. Thus, the optical bandgap of different semiconductor materials can be calculated using different equations. For indirect semiconductors, the optical bandgap can be obtained according to Tauc equation:[46]

$$\alpha(h\nu)=A(h\nu-E_g)^2 \quad (1)$$

where $\alpha(h\nu)$ is absorption coefficient (cm^{-1}), $h\nu$ is photon energy, A is constant, and E_g is optical bandgap of semiconductor. For direct semiconductor, the optical bandgap can be calculated using the following expression due to the absence of phonons in the process of photon excitation:

$$\alpha(h\nu)=A(h\nu-E_g)^{1/2} \quad (2)$$

According to the above equations, we can obtain the optical bandgap of indirect semiconductor Bi_2O_2Te and direct semiconductor Bi_2Te_3.

S6. Discussion on lattice distance and crystal orientation of Bi_2O_2Te.

According to Bragg formula, lattice distance can be calculated from the angle at XRD pattern:

$$2d\sin\theta=n\lambda \quad (3)$$

where d is lattice distance, θ is diffraction half angle, n is diffraction series (n=1, 2, 3, 4……), and λ is wavelength of target (e.g. Cu target, λ=1.54056 Å). Besides, lattice

distance can be calculated from the FFT pattern by the formula:

$$d=1/r \quad (4)$$

where d is lattice distance, and r is between bright dot and central dot (unit: nm^{-1}).

According to the tetragonal structure of Bi_2O_2Te, we can obtain the crystal orientation responding to lattice distance through the expression:

$$d= [(h/a)^2+(k/b)^2+(l/c)^2]^{-1/2} \quad (5)$$

where d is lattice distance, h, k, l represent the crystal orientation along x, y, z axis respectively, and a, b and c are the crystal parameters. Thus, we can obtain the crystal orientation responding distance according the crystal parameters of Bi_2O_2Te, and part parameters are listed in Table S1, as following:

h	k	l	D
1	0	0	0.398
0	0	1	1.27
1	1	0	0.281
1	0	1	0.38
1	1	1	0.275
2	0	0	0.199
0	0	2	0.635
2	1	0	0.178
1	0	2	0.337
2	0	1	0.197
2	2	0	0.141

2	0	2	0.19
1	1	2	0.257
2	1	1	0.176
2	2	1	0.14
2	1	2	0.171
2	2	2	0.137
3	0	0	0.133
0	0	3	0.423
3	1	0	0.126
3	0	1	0.132
1	0	3	0.29
3	2	0	0.11
3	0	2	0.13
2	0	3	0.18
3	3	0	0.094
3	0	3	0.127
3	2	1	0.11
2	1	2	0.171
3	3	1	0.094
3	1	3	0.121
3	2	2	0.109
2	2	3	0.134

3	3	2	0.093
3	2	3	0.107
3	3	3	0.092
4	0	0	0.1
0	0	4	0.318
4	1	0	0.097
4	0	1	0.099
1	0	4	0.248
4	1	1	0.096
1	1	4	0.211
4	2	0	0.089
4	0	2	0.098
2	0	4	0.169
4	2	1	0.089
4	1	2	0.095
2	1	4	0.155
4	2	2	0.088
2	2	4	0.129
4	3	0	0.08
3	0	4	0.122
4	0	3	0.097
4	3	1	0.079

4	1	3	0.094
3	1	4	0.117
4	3	2	0.079
4	2	3	0.087
3	2	4	0.104
4	3	3	0.078
3	3	4	0.09
4	4	4	0.069
5	0	0	0.08
0	0	5	0.254
6	0	0	0.066
0	0	6	0.212
7	0	0	0.057
0	0	7	0.181
8	0	0	0.05
0	0	8	0.159
9	0	0	0.044
0	0	9	0.141
0	1	0	0.398

S7. Discussion on transient response time of photodetector based on 2D Bi_2O_2Te.

Due to the internal electric field at the device, photogenerated carriers are swept to the corresponding regions of the device resulting in an increase in the mobile carriers and

hence a decrease in resistance at the device. The population and the characteristic time of these carries are denoted as n_s and τ_s, respectively. As the holes and the electrons are accumulating at the junction region, the net field at the depletion region is reduced resulting in the diffusion of electrons from one semiconductor and recombining with holes in the adjacent semiconductor. The population and the characteristic time of these diffusing electrons are denoted as n_d and τ_d, respectively. So the net increasing mobile carriers are $\Delta n = \Delta n_s e^{-t/\tau s} - \Delta n_d e^{-t/\tau d}$. Normally, τ_d is much longer than τ_s, because the holes injected into Bi_2O_2Te is assisted by the built-in field. However, according to the above discussion, we can fit the experimental data to obtain the rise (τ_r) and fall (τ_d) response time using the expressions:[47]

$$J_r = J_{r0} + Ae^{t/\tau r} \quad (6)$$

$$J_d = J_{d0} + Ae^{t/\tau d} \quad (7)$$

where J_r and J_d represent the rise and fall current density respectively, J_{r0} and J_{d0} are the maximum and minimum current density respectively, A is constant, t is time, and τ_r and τ_d are the rise and fall response time respectively.

S8. Discussion on relevant parameters of photodetector based on 2D Bi_2O_2Te.

As shown in Fig. S16, the spectra of voltage noise power density and impedance curve of the photodetector at 0 V was characterized. The current noise spectrum is shown in Fig. S17a according to the following equation:

$$i_n = V_n / R \quad (8)$$

where R is resistance of device at 0 V, i_n and V_n are current and voltage noise, respectively. As shown in Fig. S17b, the generation-recombination (g-r) noise

dominated at low frequency, while current noise decreased and temperature noise became dominant at high frequency. The characteristic frequency (f_1) can be deduced from the spectra of current noise power density. As presented in Fig. S17b, the f_1 is about 6500 Hz. Furthermore, the performance of the photodetector was independent on frequency when it was below f_1. The bandwidth frequency (Δf) was that of the lock-in amplifier at 1 Hz. Since g-r noise dominated the photodetector, the current noise should be selected from the plateau region when evaluating the performances of the photodetector, such as noise equivalent power density (NEP) and detectivity (D^*) using the following equations:[48-51]

$$\mathrm{NEP}=i_n/R_i \quad (9)$$

$$D^*=(A_D\Delta f)^{1/2}/\mathrm{NEP} \quad (10)$$

where i_n and R_i are current noise and responsivity without bias voltage, respectively. A_D and Δf are active area and bandwidth of the photodetector, respectively. Due to the independent relationship between responsivity and frequency, the responsivity spectrum at 0 V was shown in Fig. S17a according to Fig. 4d. The plot of detectivity of the photodetector at 0V in Fig. S17c was obtained through measurement at DC mode. Besides, the detectivity and NEP were also characterized in AC mode by measuring current noise using a lock-in amplifier (HF2LI). On basis of equation (9) and (10), the current noise at 6500 Hz was selected (as shown in Fig. S17b). Both NEP and detectivity spectra are shown in Fig. S17d. When comparing the detectivity spectra under AC and DC modes, it can be concluded that the current noise of the 2D Bi_2O_2Te based photodetector was dominated by g-r noise and the photodetector

exhibited equivalent performances under AC and DC modes of operation.

S9. Table on a list of Hall measurements on sputtered Bi_2Te_3 (Table S2).

Sputtering time (Seconds)	Resistivity (Ω·cm)	Hall coefficient (cm^3C^{-1})	Carrier concentration (cm^{-3})	Mobility ($cm^2V^{-1}s^{-1}$)	Conduction type(N/P)
1	$6.07x10^{-3}$	$-1.1x10^{-2}$	$5.69x10^{20}$	1.81	N
5	$2.81x10^{-3}$	$-5.13x10^{-3}$	$1.22x10^{21}$	1.82	N
10	$6.2x10^{-3}$	$-1.47x10^{-2}$	$4.23x10^{20}$	2.38	N
15	$3.6x10^{-3}$	$-1.42x10^{-2}$	$4.41x10^{20}$	3.93	N
20	$4.3x10^{-3}$	$-7.22x10^{-3}$	$8.65x10^{20}$	1.67	N
30	$3.1x10^{-3}$	$-8.75x10^{-3}$	$7.13x10^{20}$	2.83	N
45	$9.0x10^{-3}$	$-1.29x10^{-2}$	$4.84x10^{20}$	1.43	N
60	$2.1x10^{-3}$	$-2.94x10^{-2}$	$2.12x10^{20}$	1.40	N

Supplementary References

1. Chen, Y. L. et al. Experimental realization of a three-dimensional topological insulator, Bi_2Te_3. *Science* 2009, **325**, 178-180.
2. Song, J. et al. Monolayer and few-layer all-inorganic perovskites as a new family of two-dimensional semiconductors for printable optoelectronic devices. *Adv. Mater.* 2016, **28**, 4861-4869.
3. Wang, X. et al. Ultrasensitive and broadband MoS_2 photodetector driven by ferroelectrics. *Adv. Mater.* 2015, **27**, 6575-6581.
4. Xie, C., Mak, C., Tao, X. & Yan, F. Photodetectors based on two-dimensional

layered materials beyond graphene. *Adv. Funct. Mater.* 2017, **27**, 1603886.

5. Huang, M. et al. Broadband black-phosphorus photodetectors with high responsivity. *Adv. Mater.* 2016, **28**, 3481-3485.
6. Zhang, Q. et al. 2D semiconductors towards high-performance ultraviolet photodetection. *J. Phys. D: Appl. Phys.* 2019, **52**, 303002.
7. Hao, L. et al. 2D SnSe/Si heterojunction for self-driven broadband photodetectors. *2D Mater.* 2019, **6**, 034004.
8. Hu, Z. et al. Recent progress in 2D group IV-IV monochalcogenides: synthesis, properties and applications. *Nanotechnol.* 2019, **30**, 252001.
9. Zhang, S. et al. Ultrasensitive hybrid MoS_2-ZnCdSe quantum dot photodetectors with high gain. *ACS Appl. Mater. & Interfaces* 2019, **11**, 23667-23672.
10. Wang, B. et al. Broadband photodetectors based on 2D group IVA metal chalcogenides semiconductors. *Appl. Mater. Today* 2019, **15**, 115-138.
11. Yin, Y. et al. High-speed and high-responsivity hybrid silicon/black-phosphorus waveguide photodetectors at 2 μm. *Laser & Photon. Rev.* 2019, **13**, 1900032.
12. Zhang, X. et al. Edge-state-enhanced ultrahigh photoresponsivity of graphene nanosheet-embedded carbon film/silicon heterojunction. *Adv. Mater. Interfaces*2019, 1802062.
13. Wang, F. et al. 2D metal chalcogenides for IR photodetection. *Small* 2019, **15**, 1901347.
14. Long, M., Wang, P., Fang, H. & Hu, W. Progress, challenges, and opportunities for 2D material based photodetectors. *Adv. Funct. Mater.* 2018, **29**, 1803807.

15. Zeng, W. et al. Synthesis of large-area atomically thin BiOI crystals with highly sensitive and controllable photodetection. *Adv. Funct. Mater.* 2019, **29**, 1900129.

16. Zheng, Y. et al. Self-integrated hybrid ultraviolet photodetectors based on the vertically aligned InGaN nanorod array assembly on graphene. *ACS Appl. Mater. & Interfaces* 2019, **11**, 13589-13597.

17. Alsaif, M. et al. 2D SnO/In_2O_3 van der Waals heterostructure photodetector based on printed oxide skin of liquid metals. *Adv. Mater. Interfaces* 2019, **6**, 1900007.

18. Khan, U. et al. Controlled vapor-solid deposition of millimeter-size single crystal 2D Bi_2O_2Se for high-performance phototransistors. *Adv. Funct. Mater.* 2019, **29**, 1807979.

19. Kim, Y., Bark, H., Kang, B. & Lee, C. Wafer-scale substitutional doping of monolayer MoS_2 films for high-performance optoelectronic devices. *ACS Appl. Mater. & Interfaces* 2019, **11**, 12613-12621.

20. Hu, A. et al. Graphene on self-assembled InGaN quantum dots enabling ultrahighly sensitive photodetectors. *Adv. Opt. Mater.* 2019, **7**, 1801792.

21. Zhang, K. et al. A substrate-enhanced MoS_2 photodetector through a dual-photogating effect. *Mater. Horiz.* 2019, **6**, 826-833.

22. You, C. et al. Cascade-type energy band design of a black phosphorus photodetector with high performance. *J. Mater. Chem. C* 2019, **7**, 2232-2239.

23. Chen, D. R. et al. Lateral two-dimensional material heterojunction photodetectors with ultrahigh speed and detectivity. *ACS Appl. Mater. & Interfaces* 2019, **11**, 6384-6388.

24. Li, A. et al. Ultrahigh-sensitive broadband photodetectors based on dielectric shielded $MoTe_2$/Graphene/SnS_2 p-g-n junctions. *Adv. Mater.* 2019, **31**, 1805656.

25. Ulaganathan, R. K., Yadav, K., Sankar, R., Chou, F.C. & Chen Y.-T. Hybrid InSe nanosheets and MoS_2 quantum dots for high-performance broadband photodetectors and photovoltaic cells. *Adv. Mater. Interfaces* 2018, 1801336.

26. Zeng, L.-H. et al. Controlled synthesis of 2D palladium diselenide for sensitive photodetector applications. *Adv. Funct. Mater.* 2019, **29**, 1806878.

27. Fu, Q. et al. Ultrasensitive 2D Bi_2O_2Se phototransistors on silicon substrates. *Adv. Mater.* 2019, **31**, 1804945.

28. Liu, T., Tong, L., Huang, X. & Ye, L. Room-temperature infrared photodetectors with hybrid structure based on two-dimensional materials. *Chin. Phys. B* 2019, **28**, 017302.

29. Wang, F. et al. Liquid-alloy-assisted growth of 2D ternary $Ga_2In_4S_9$ toward high-performance UV photodetection. *Adv. Mater.* 2019, **31**, 1806306.

30. Yu, M. et al. Synthesis of two-dimensional alloy $Ga_{0.84}In_{0.16}Se$ nanosheets for high-performance photodetector. *ACS Appl. Mater. & Interfaces* 2018, **10**, 43299-43304.

31. Peng, M. et al. PbS quantum dots/2D nonlayered CdS_xSe_{1-x} nanosheet hybrid nanostructure for high-performance broadband photodetectors. *ACS Appl. Mater. & Interfaces* 2018, **10**, 43887-43895.

32. Lu, J. et al. Graphene/In_2S_3 van der Waals heterostructure for ultrasensitive photodetection. *ACS Photon.* 2018, **5**, 4912-4919.

33. Qin, J. K. et al. Epitaxial growth of 1D atomic chain based Se nanoplates on monolayer ReS_2 for high-performance photodetectors. *Adv. Funct. Mater*. 2018, **28**, 1806254.

34. Hu, X. et al. Halide-induced self-limited growth of ultrathin nonlayered Ge flakes for high-performance phototransistors. *J. Am. Chem. Soc.* 2018, **140**, 12909-12914.

35. Patel, M., Kim, J. & Kim, Y. K. Growth of large-area SnS films with oriented 2D SnS layers for energy-efficient broadband optoelectronics. *Adv. Funct. Mater.* 2018, **28**, 1804737.

36. Cao, S. et al. Ultrahigh-photoresponsive UV photodetector based on a BP/ReS_2 heterostructure p-n diode. *Nanoscale* 2018, **10**, 16805-16811.

37. Deng, W. et al. High detectivity from a lateral graphene-MoS_2 schottky photodetector grown by chemical vapor deposition. *Adv. Electron. Mater.* 2018, **4**, 1800069.

38. Wu, D. et al. Design of 2D layered $PtSe_2$ heterojunction for the high-performance, room-temperature, broadband, infrared photodetector. *ACS Photon.* 2018, **5**, 3820-3827.

39. Wang, F. et al. 2D library beyond graphene and transition metal dichalcogenides: a focus on photodetection. *Chem. Soc. Rev.* 2018, **47**, 6296-6341.

40. Wang, F. et al. Submillimeter 2D Bi_2Se_3 flakes toward high-performance infrared photodetection at optical communication wavelength. *Adv. Funct. Mater.* 2018, **28**, 1802707.

41. Yang, M. et al. Enhanced performance of wideband room temperature

photodetector based on Cd_3As_2 thin film/pentacene heterojunction. *ACS Photon.* 2018, **5**, 3438-3445.

42. Amani, M. et al. Solution-synthesized high-mobility tellurium nanoflakes for short-wave infrared photodetectors. *ACS Nano* 2018, **12**, 7253-7263.
43. Gao, Y. et al. Bias-switchable negative and positive photoconductivity in 2D $FePS_3$ ultraviolet photodetectors. *Nanotechnol.* 2018, **29**, 244001.
44. Qiao, J., Kong, X., Hu, Z.-X., Yang, F. & Ji, W. High-mobility transport anisotropy and linear dichroism in few-layer black phosphorus. *Nat. Comm.* 2014, **5**, 4475.
45. Duan, Y., Qin, L., Shi, L., Tang, G. & Shi, H. Hybrid density functional theory study of band gap tuning in AlN and GaN through equibiaxial strains. *Appl. Phys. Lett.* 2012, **100**, 022104.
46. Wang, W. et al. Crystal field splitting and optical bandgap of hexagonal $LuFeO_3$ films. *Appl. Phys. Lett.* 2012, **101**, 241907.
47. Cai, Y. et al. High performance ultraviolet photodetectors based on ZnO nanoflakes/PVK heterojunction. *Appl. Phys. Lett.* 2016, **109**, 073103.
48. Maiti, R. et al. Strain-engineered high-responsivity $MoTe_2$ photodetector for silicon photonic integrated circuits. *Nat. Photon.* 2020, https://doi.org/10.1038/s41566-020-0647-4 1749-4893.
49. Yin, C. et al. Ultrabroadband photodetectors up to 10.6 μm based on 2D Fe_3O_4 nanosheets. *Adv. Mater.* 2020, **32**, 2002237.
50. Huang, J. et al. A high-performance solution-processed organic photodetector for

near-infrared sensing. *Adv. Mater.* 2019, **32**, 1906027.

51. Li, C. et al. Ultrafast and broadband photodetectors based on a perovskite/organic bulk heterojunction for large-dynamic-range imaging. *Light: Sci. & Appl.* 2020, **9**, 31.